

## Large spin-driven dielectric response and magnetoelectric coupling in the buckled honeycomb $\text{Fe}_4\text{Nb}_2\text{O}_9$

Lei Ding <sup>1,\*</sup>, Minseong Lee <sup>2</sup>, Eun Sang Choi,<sup>2</sup> Jing Zhang,<sup>3</sup> Yan Wu <sup>1</sup>, Ryan Sinclair,<sup>4</sup> Bryan C. Chakoumakos <sup>1</sup>,  
Yisheng Chai,<sup>3</sup> Haidong Zhou <sup>4,2</sup> and Huibo Cao <sup>1,†</sup>

<sup>1</sup>Neutron Scattering Division, Oak Ridge National Laboratory, Oak Ridge, Tennessee 37831, USA

<sup>2</sup>National High Magnetic Field Laboratory, Florida State University, Tallahassee, Florida 32306-4005, USA

<sup>3</sup>Low Temperature Physics Laboratory, College of Physics, Chongqing University, Chongqing 401331, China

<sup>4</sup>Department of Physics and Astronomy, University of Tennessee, Knoxville, Tennessee 37996-1200, USA



(Received 1 May 2020; revised 21 June 2020; accepted 7 July 2020; published 6 August 2020)

We present the significant spin-driven dielectric anomaly ( $\sim 40\%$  drop) and magnetoelectric coupling near the magnetic ordering temperature in single crystal  $\text{Fe}_4\text{Nb}_2\text{O}_9$ . By combining neutron and x-ray single crystal diffraction techniques, we unambiguously determined its magnetic symmetry and studied the structural phase transition at  $T_S = 70$  K. The temperature-dependent static dielectric constant is strongly anisotropic, rendering two dielectric anomalies along the  $a$  axis in the hexagonal lattice with the first one coupled to the magnetic ordering around  $T_N = 97$  K and the second one accompanying with a first-order structural transition around  $T_S = 70$  K. Below  $T_N$ , we found that the anomalous dielectric constant is practically proportional to the square of the magnetic moment from neutron diffraction data, indicating that the exchange striction is likely responsible for the strong spin-lattice coupling. Magnetic-field-induced magnetoelectric coupling was observed and is compatible with the determined magnetic structure that is characteristic of antiferromagnetically arranged ferromagnetic chains in the honeycomb plane. We propose that such magnetic symmetry should be immune to external magnetic fields to some extent favored by the freedom of rotation of moments in the honeycomb plane, laying out a promising system to control the magnetoelectric properties by magnetic fields.

DOI: [10.1103/PhysRevMaterials.4.084403](https://doi.org/10.1103/PhysRevMaterials.4.084403)

### I. INTRODUCTION

The linear magnetoelectric (ME) effect, which defines the control of electric polarization by an external magnetic field or the magnetization by an electric field [1,2], has attracted considerable interest because of its importance in understanding the novel types of ferroic order [3–6] in solids and potential applications in spintronics [4,7–10]. For the presence of the linear ME effect in a specific material, the symmetry requires the breaking of both spatial inversion and time reversal [3]. In this regards, the linear ME effect can be predicted by symmetry considerations given the magnetic symmetry of a system is clearly known [1,11]. A family of materials  $\text{A}_4\text{Nb}_2\text{O}_9$  ( $\text{A} = \text{Mn}, \text{Co}$ ) belonging to the corundum-type structure has been found in their powder forms to show the magnetoelectric effect for several decades [12]. They crystallize with the  $\alpha\text{-Al}_2\text{O}_3$ -type trigonal crystal structure with the space group  $P\bar{3}c1$  [13,14] [see Figs. 1(a) and 1(b)] and can be regarded as a derivative of  $\text{Cr}_2\text{O}_3$ , one of the first predicted and discovered room temperature ME materials [15–19]. The magnetic structures of both Mn and Co cases were first determined by Bertaut *et al.* in Ref. [14] where both of them can be simply described by an antiferromagnetically coupled collinear ferromagnetic  $\text{Co}^{2+}$  chains with the moments along

the  $c$ -axis. Originally, this symmetry allows a linear ME effect and seems to be consistent with the observed linear ME response in the powder samples [12,20,21].

Recently, this family has attracted some renewed interest because of the successful growth of  $\text{Co}_4\text{Nb}_2\text{O}_9$  single crystals and the finding of manipulations of its ME effect via external magnetic fields [22]. Single crystal neutron diffraction experiments have revealed a different magnetic structure with all moments in the  $ab$  plane [23]. This allows different magnetoelectric effect terms as observed in the electric polarization measurement on a single crystal [13,23,24].  $\text{Fe}_4\text{Nb}_2\text{O}_9$  emerging as a new member in this family was recently reported to show the magnetoelectric coupling accompanied by a long-range antiferromagnetic ordering below 90 K and an anomaly at 77 K in the dielectric permittivity curve on a powder sample [25]. It was later shown in Ref. [26] that the magnetic structure is described by collinearly arranged moments in the  $ab$  plane which can be assigned in either  $C2/c'$  or  $C2'/c$  magnetic symmetry through a powder neutron diffraction experiment. To elucidate the exact magnetic symmetry that is vital in explaining the magnetoelectric coupling, single crystal neutron diffraction is required.

In contrast to the previous works on a powder  $\text{Fe}_4\text{Nb}_2\text{O}_9$  sample, in this work, the availability of the sizable single crystal allows us to study the magnetoelectric coupling in different crystal directions and elucidate the magnetic ground state using the single crystal neutron diffraction technique. We show the large spin-driven dielectric anomaly in the

\*dingl@ornl.gov

†caoh@ornl.gov

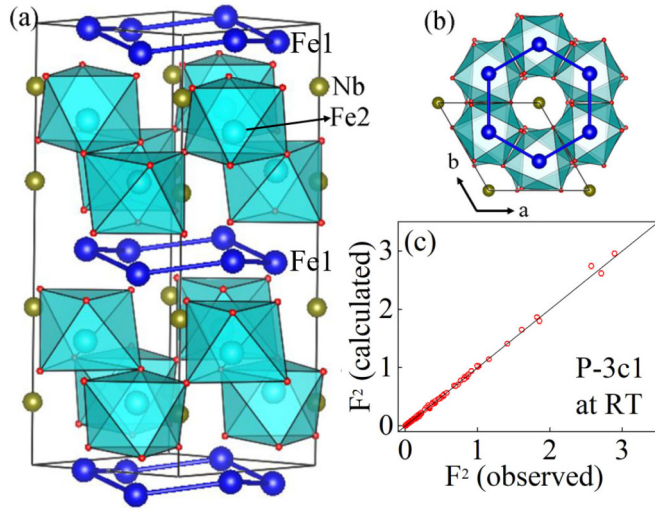


FIG. 1. (a) Schematic drawing of the crystal structure of Fe<sub>4</sub>Nb<sub>2</sub>O<sub>9</sub> at room temperature viewing along the [110] direction. (b) The slightly buckled honeycomb layer is formed by Fe1 atoms. (c) Observed and calculated single crystal x-ray diffraction data at room temperature with the goodness-of-fit  $\chi^2 = 0.94$  and  $R$  factor  $R_{F_2} = 3.15\%$ .

dielectric constant curves that exhibit the obvious anisotropy, and the observation of electric polarization under the applied magnetic field around the Néel temperature in Fe<sub>4</sub>Nb<sub>2</sub>O<sub>9</sub>. The observed magnetoelectric coupling is in good agreement with the determined magnetic symmetry  $C2/c'$  that allows the presence of linear ME effect with both diagonal and off-diagonal components.

## II. EXPERIMENTAL METHODS

Single crystals of Fe<sub>4</sub>Nb<sub>2</sub>O<sub>9</sub> were grown by the traveling-solvent floating-zone (TSFZ) technique. The feed and seed rods for the crystal growth were prepared by solid state reaction. Appropriate mixtures of Fe<sub>2</sub>O<sub>3</sub>, Fe, and Nb<sub>2</sub>O<sub>5</sub> were ground together and pressed into 6-mm diameter  $\times$  60 mm rods under 400-atm hydrostatic pressure and then calcined in argon at 1100 C for 24 h. The crystal growth was carried out in argon in an IR-heated image furnace (NEC) equipped with two halogen lamps and double ellipsoidal mirrors with feed and seed rods rotating in opposite directions at 25 rpm during crystal growth at a rate of 4 mm/h.

Single-crystal x-ray diffraction data were collected down to 40 K using a Rigaku XtaLAB PRO diffractometer with the graphite monochromated Mo  $K_\alpha$  radiation ( $\lambda = 0.71073$  Å) equipped with a HyPix-6000HE detector and an Oxford N-HeliX cryocooler. Peak indexing and integration were done using the RIGAKU OXFORD DIFFRACTION CRYCALISPRO software [27]. An empirical absorption correction was applied using the SCALE3 ABSPACK algorithm as implemented in CRYCALISPRO. [28]. Structure refinement was done using FULLPROF Suite [29].

The dc magnetization curves were obtained using the magnetic property measurement system (MPMS) superconducting quantum interference device (SQUID) magnetometer from Quantum Design. For the dielectric constant

measurements, single crystals were used whose orientations were determined by Laue diffraction. Two single crystalline samples were polished to achieve two parallel flat surfaces perpendicular to the  $a$  and  $c$  axes, respectively. An Andeen-Hagerling AH-2700A commercial capacitance bridge was used to measure the capacitance, which was converted to dielectric constant. This measurement employed electric fields of 21 and 14.6 kV/m for  $E\parallel a$  and  $E\parallel c$  configuration, respectively.

The temperature dependence of electric polarization was measured under various magnetic fields. Prior to the pyroelectric current measurements, the crystal was subjected to a magnetoelectric annealing procedure to obtain a single magnetic domain. This procedure was performed by cooling the sample from 99 to 77 K with the simultaneously applied magnetic field  $H\parallel a$  and electric field  $E\parallel c$  ( $E = \pm 183$  kV/m). For the measurement of reverse magnetic field, a magnetic field sweeping from 9 to  $-9$  T at 77 K was employed. Then, the electric field  $E$  was turned off at 77 K, and the electrodes were shorted. The pyroelectric current was recorded on warming at a rate of 1 K/min from 77 to 99 K using a Keithley 6517B electrometer. The electric polarization was calculated by integrating the measured pyroelectric current as a function of time.

Single-crystal neutron diffraction was performed at the HB-3A Four-Circle Diffractometer (FCD) equipped with a two-dimensional (2D) detector at the High Flux Isotope Reactor (HFIR) at Oak Ridge National Laboratory (ORNL). Neutron wavelength of 1.003 Å (neutron energy 81 meV) was used with a bent perfect Si-331 monochromator [30]. The nuclear and magnetic structure refinements were performed using the FULLPROF suite package [29].

## III. RESULTS

### A. Crystal structure at room temperature

The availability of single crystal Fe<sub>4</sub>Nb<sub>2</sub>O<sub>9</sub> enabled us to carefully examine its crystal structure using both single crystal neutron and x-ray diffraction techniques, hence providing more precise structural parameters. Room temperature x-ray single crystal diffraction data show that Fe<sub>4</sub>Nb<sub>2</sub>O<sub>9</sub> crystallizes with the space group  $P\bar{3}c1$ , in good agreement with the previous reports [25,26]. The refinement result based on the x-ray diffraction data with a comparison between the observed and the calculated squared structure factor is shown in Fig. 1(c). Single crystal neutron diffraction at 120 K confirms the space group  $P\bar{3}c1$  and indicates a good quality of the single crystal. The refined structural parameters were summarized in Table I. As shown in Fig. 1, the crystal structure is characterized by an alternate stacking of slightly buckled Fe1O<sub>6</sub> honeycomb and strongly buckled Fe2O<sub>6</sub> honeycomb layers along the  $c$  axis. The nearest-neighbor interactions ( $J_1$ ) between Fe cations are along the  $c$  axis with the Fe1-Fe2 distance  $d_1 = 2.979(1)$  Å through a superexchange path Fe1-O1-Fe2 [91.8(2) $^\circ$ ] between the two edge-sharing FeO<sub>6</sub> as shown in Fig. 8(c).

### B. Magnetic, dielectric properties, and magnetoelectric coupling

The magnetic susceptibility of a Fe<sub>4</sub>Nb<sub>2</sub>O<sub>9</sub> single crystal was measured with both zero field cooling (ZFC) and field

TABLE I. The refined structural parameters of  $\text{Fe}_4\text{Nb}_2\text{O}_9$  based on both single-crystal x-ray diffraction (XRD) at room temperature and neutron diffraction (ND) data at 120 K. [Space group:  $P\bar{3}c1$ ,  $a = b = 5.2118(3)\text{\AA}$ ,  $c = 14.2037(8)\text{\AA}$ ,  $R_{p2}(\text{x-ray}) = 3.15\%$ ,  $R_{p2}(\text{neutron}) = 6.76\%$ ,  $B_{\text{iso}}$  in  $1/(8\pi^2)\text{\AA}^2$ ].

Atom	methods	x	y	z	$B_{\text{iso}}$
Nb1	XRD	0	0	0.14251(6)	0.56(1)
	ND			0.14266(2)	0.67(8)
Fe2	XRD	1/3	2/3	0.19325(6)	0.77(2)
	ND			0.1933(2)	0.82(8)
Fe1	XRD	1/3	2/3	0.98522(6)	0.72(2)
	ND			0.9860(1)	0.61(7)
O1	XRD	0.6625(6)	0.9767(7)	0.0847(2)	0.85(5)
	ND	0.6609(3)	0.9763(5)	0.0852(1)	0.72(7)
O2	XRD	0.2837(9)	0	1/4	0.75(6)
	ND	0.2853(6)			0.64(8)

cooling (FC) protocols on heating along the  $a$  and  $c$  axes. The evident difference between the magnetic susceptibility curves along the two directions indicates a strong easy-plane anisotropy. This suggests that the magnetic moments are largely constrained in the  $ab$  plane. Upon cooling, a single anomaly around 93 K featured by a bifurcation between ZFC and FC curves was observed for both directions (Fig. 2), which is indicative of a long-range antiferromagnetic transition around  $T_N = 97$  K shown in the neutron diffraction section, in accordance with the results previously reported on powder samples [25,26]. A rather small upturn below 5 K is probably due to the presence of the impurity  $\text{FeNb}_2\text{O}_6$  [31] that is too small to be detected by the x-ray and neutron diffraction techniques.

To study the dielectric properties of  $\text{Fe}_4\text{Nb}_2\text{O}_9$ , the frequency-dependent dielectric constants ( $\epsilon'$ ) were measured on the single crystal with an electric field along the  $a$  or  $c$  axis. As shown in Fig. 3, the dielectric constant  $\epsilon'(T)$  along the  $a$  axis is much larger than that along the  $c$  axis, reflecting

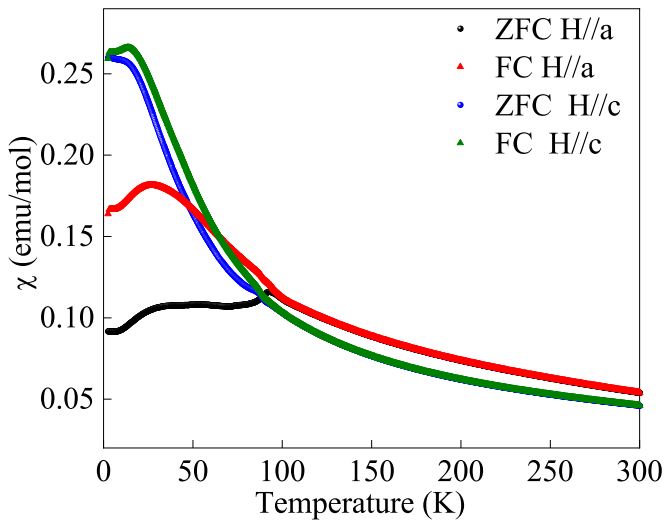


FIG. 2. Temperature dependence of the magnetic susceptibility of  $\text{Fe}_4\text{Nb}_2\text{O}_9$  with a magnetic field  $\mu_0H = 0.2$  T parallel to the  $a$  and  $c$  axes under both ZFC and FC protocols.

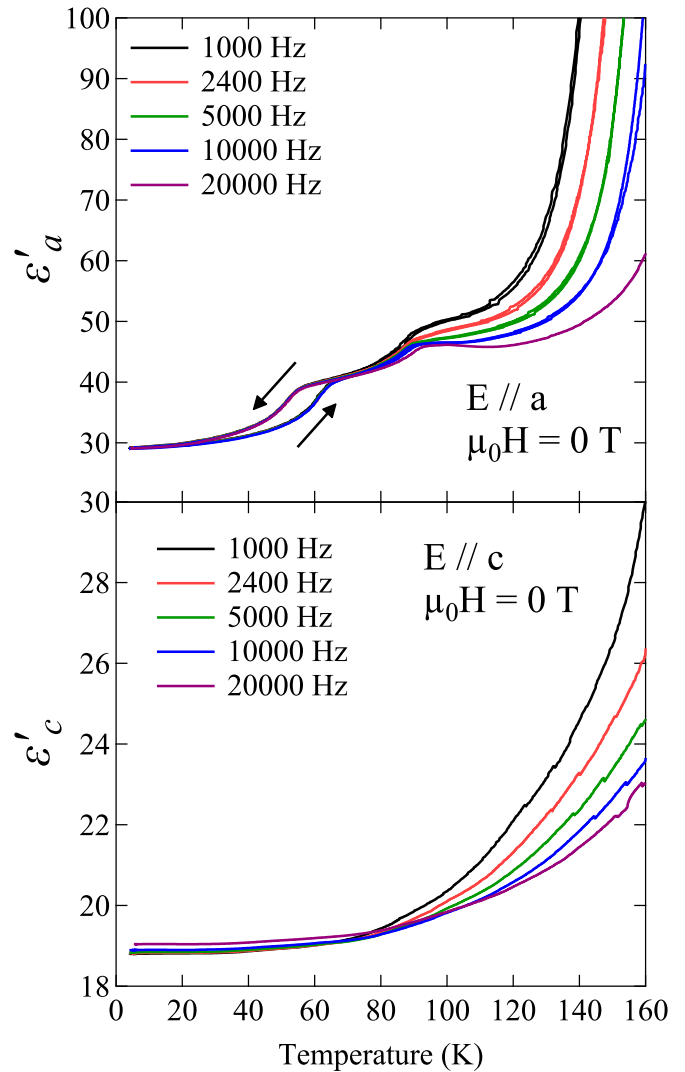


FIG. 3. The temperature-dependent dielectric constant at various frequencies with the electric field  $E$  parallel to the  $a$  and  $c$  axes, respectively.

the presence of strong anisotropy of dielectric properties in  $\text{Fe}_4\text{Nb}_2\text{O}_9$ . This is in fact consistent with the magnetic easy-plane anisotropy observed in the magnetic susceptibility curves. An anomalous change in the slope of dielectric constant is clearly discerned occurring at the Néel temperature for  $E||a$ , but is invisible for  $E||c$ . The in-plane dielectric constant signals a much more sensitive response to the spin ordering than the magnetic susceptibility. On further cooling, both  $\epsilon'_a(T)$  and  $\epsilon'_c(T)$  curves decrease. However, only  $\epsilon'_a(T)$  shows an obvious bump around  $T_S = 70$  K, which is accompanied by a considerable thermal hysteresis behavior. This suggests the first-order nature of the crystal structural transition also observed in the previous work [26]. Below  $T_N$  the dielectric constant reduces greatly and yields a significant drop ( $\sim 40\%$ ) as the temperature is lowered to 4.2 K. This dielectric response to the spin ordering, as will be discussed later, is substantially larger than that in antiferromagnets reported hitherto, indicating a strong correlation between magnetism and the dielectric properties in  $\text{Fe}_4\text{Nb}_2\text{O}_9$ .

TABLE II. The refined structural parameters of  $\text{Fe}_4\text{Nb}_2\text{O}_9$  with single crystal x-ray diffraction data at 40 K. Space group:  $C2/c$ , lattice parameters  $a = 9.0861(6)\text{\AA}$ ,  $b = 5.1970(4)\text{\AA}$ ,  $c = 14.234(1)\text{\AA}$ ,  $\beta = 91.294(3)^\circ$ .  $\chi^2 = 1.45$ .  $B_{\text{iso}}$  has unit of  $1/(8\pi^2)\text{\AA}^2$ .

Atom	$x$	$y$	$z$	$B_{\text{iso}}$
Nb1	0.0010(3)	-0.0004(3)	0.64284(6)	0.87(2)
Fe2	0.8325(4)	0.4994(4)	0.6926(1)	0.85(3)
Fe1	0.8337(4)	0.5001(4)	0.4855(1)	0.86(3)
O1	0.845(3)	0.821(2)	0.0863(9)	0.7(2)
O2	0.672(3)	0.355(2)	0.0858(8)	1.5(2)
O3	0.986(3)	0.328(2)	0.0833(8)	0.7(1)
O4	0	0.722(2)	1/4	0.7(2)
O5	0.141(3)	0.145(2)	0.250(1)	0.9(2)

Magnetodielectric response was considered to be a definitive and experimentally accessible method to recognize linear magnetoelectric materials [32]. This method can circumvent the experimental difficulties typically in the pyroelectric current measurements. We thus evaluated the magnetoelectric coupling in  $\text{Fe}_4\text{Nb}_2\text{O}_9$  single crystal by measuring the magnetodielectric response. Figure 4 shows the dielectric constant as a function of magnetic field with a fixed frequency  $f=20\text{ kHz}$ . Three configurations  $E\parallel H\parallel a$ ,  $E\parallel H\parallel c$ , and  $E\parallel c$ ,  $H\parallel a$  were used to measure the magnetodielectric response. For the configuration  $E\parallel c$ ,  $H\parallel a$ , a peak in the  $\varepsilon'(T)$  curve was observed around  $T_N$ , which becomes stronger with increasing magnetic field. A small magnetic-field-induced change at  $T_N$  in the  $\varepsilon'(T)$  was observed for  $E\parallel H\parallel a$  configuration. The applied magnetic field up to 7 T does not affect the thermal hysteresis around  $T_S$ . No anomaly was observed up to 7 T for  $E\parallel H\parallel c$  configuration. These observations indicate a considerable magnetoelectric coupling in  $\text{Fe}_4\text{Nb}_2\text{O}_9$ . Note that the dielectric constant decreases at high temperatures when applying the magnetic field. This discrepancy seems considerable at high temperatures and can be attributed to the existence of the conductivity from impurity or thermally excited carriers.

To study the ME coupling, we measured the electric polarization of  $\text{Fe}_4\text{Nb}_2\text{O}_9$ . Figure 5 shows the temperature dependence of the pyroelectric current and polarization at different magnetic fields with  $E\parallel c$ ,  $H\parallel a$ . For the measured current in the absence of the magnetic field, we observed a broad bump across the magnetic transition that we considered as a background signal. No peak in the pyroelectric current curve was observed in the absence of an external magnetic field, suggesting that  $\text{Fe}_4\text{Nb}_2\text{O}_9$  is not polar around the magnetic phase transition. However, when a magnetic field of 4 T is applied, the induced current appears in the vicinity of the magnetic phase transition. The induced current becomes stronger with increasing magnetic field. By reversing the annealing electric field, we were able to change the sign of the induced current. The temperature dependence of electric polarization was then obtained by integrating the pyroelectric current with respect to the time. As shown in the lower panel in Fig. 5, the electric polarization monotonically increases with the increase of the magnetic field. The observed maximum polarization value is about  $32\text{ }\mu\text{C}/\text{m}^2$  under 9 T, comparable to that

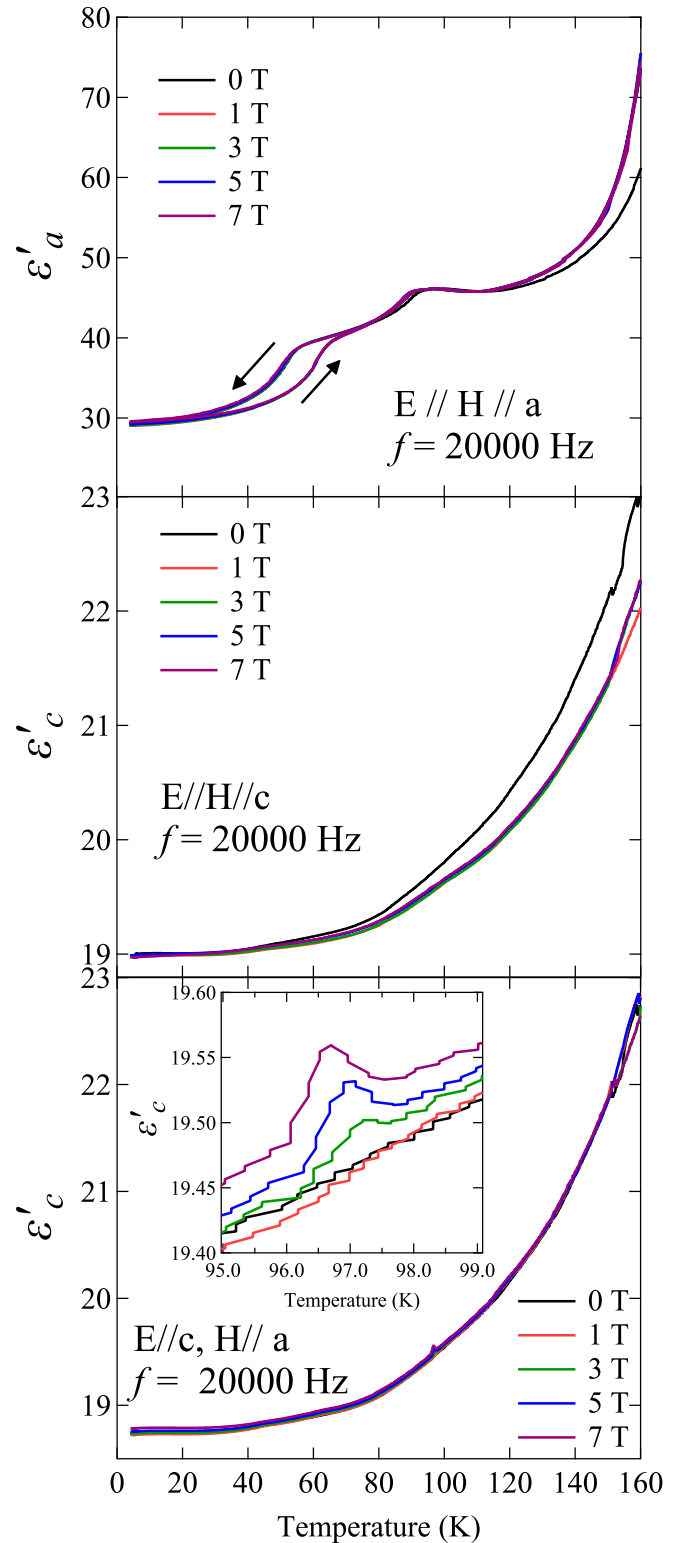


FIG. 4. Magnetic field dependence of the dielectric constant of  $\text{Fe}_4\text{Nb}_2\text{O}_9$  with magnetic and electric fields applied to different configurations. Inset shows the magnified view of the magnetoelectric coupling.

in the counterpart magnetoelectric  $\text{Co}_4\text{Nb}_2\text{O}_9$  [13,23] in the same magnetic and electric configuration. A magnetic-field-dependent polarization curve apparently reveals the linear feature, reflecting that the linear ME effect is dominant in

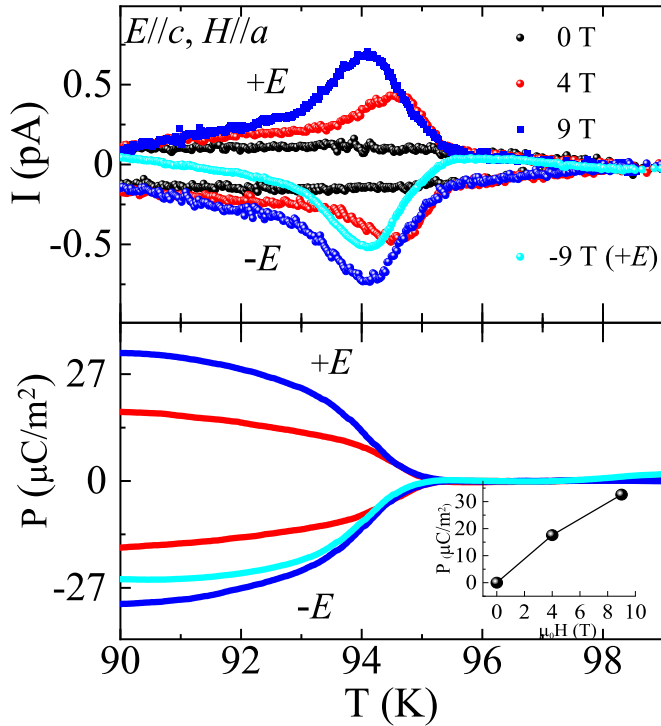


FIG. 5. Temperature dependence of the pyroelectric current (top panel) and the corresponding polarization (bottom panel) under various magnetic fields. The observable magnetoelectric coupling occurs below 96 K, close to the magnetic transition temperature of 97 K. Inset shows the linear behavior of the polarization as a function of magnetic field.

$\text{Fe}_4\text{Nb}_2\text{O}_9$ . We also examined the influence of the reverse magnetic field on the electric polarization. As shown in Fig. 5, a reverse magnetic field of 9 T can make the polarization reverse. Note that the bump feature in the absence of magnetic field is not reversed, indicating the background nature of the  $\mu_0H = 0$  T data.

**C. Low temperature crystal and magnetic structures determination**

To check the crystal structure at low temperatures, we performed single crystal x-ray (down to 40 K) and neutron diffraction (down to 5 K) experiments at various temperatures. For the neutron diffraction data, rocking curve scans around Bragg peaks (0 1 0), (0 2 0), (0 3 0), and (1 1 3) at 5 K reveal obvious peak splittings, indicating a monoclinic structural transition [26]. Two representative reflections (0 1 0) and (0 2 0) as a function of temperature are shown in Figs. 7(a) and 7(b). To solve the crystal structure at low temperatures, we performed the group-subgroup analysis using tools at the Bilbao Crystallographic Server. In a sort of symmetry-related maximal subgroups of  $P\bar{3}c1$ , only subgroup  $C2/c$  with the index of 3 is monoclinic. The structure was then refined in this space group using the single crystal x-ray diffraction data at 40 K (Table II). Figure 6 shows the result of the refinement ( $\chi^2 = 1.45$ ) as well as the schematic drawings of the corresponding crystal structure at 40 K. It appears that the crystal structure at 40 K is just slightly distorted from the high

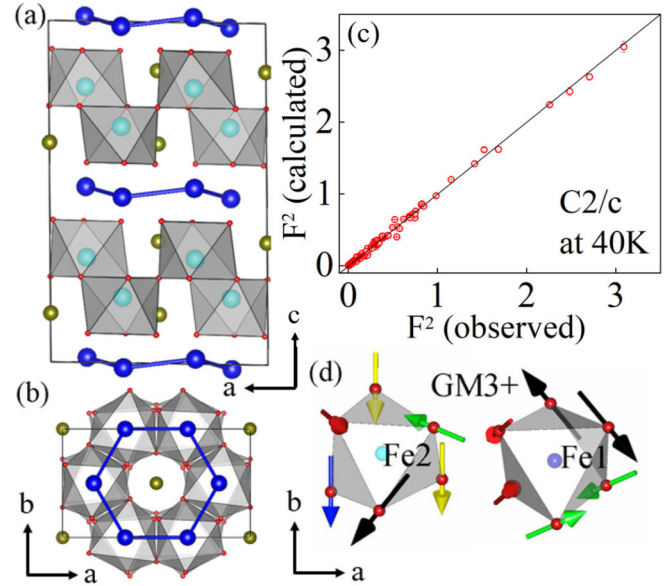


FIG. 6. (a, b) Crystal structure of  $\text{Fe}_4\text{Nb}_2\text{O}_9$  projected along the  $b$  and  $c$  directions. (c) Observed structure factor squared values of diffraction peaks compared to those calculated by fitting the  $C2/c$  monoclinic structural model at 40 K with the goodness-of-fit  $\chi^2 = 1.45$  and  $R$  factor  $R_{F2} = 5.86\%$ . (d) Visualization of the atomic displacements of the primary  $\text{GM}3+$  irrep (amplitude: 0.1124 Å) from the symmetry adapted mode analysis projected into the  $ab$  plane, accounting for the  $P\bar{3}c1$  to  $C2/c$  transition. Arrows denote the polarization vectors of the symmetry modes of the O atomic displacements with moduli proportional to the amplitude.

temperature phase. Atoms O1 and O2 in the  $P\bar{3}c1$  structure were split into five atomic positions in the low temperature phase, demonstrating the largest atomic displacements. To illustrate the O atomic displacements compared to the parent structure ( $P\bar{3}c1$ ) we conducted the symmetry mode analysis

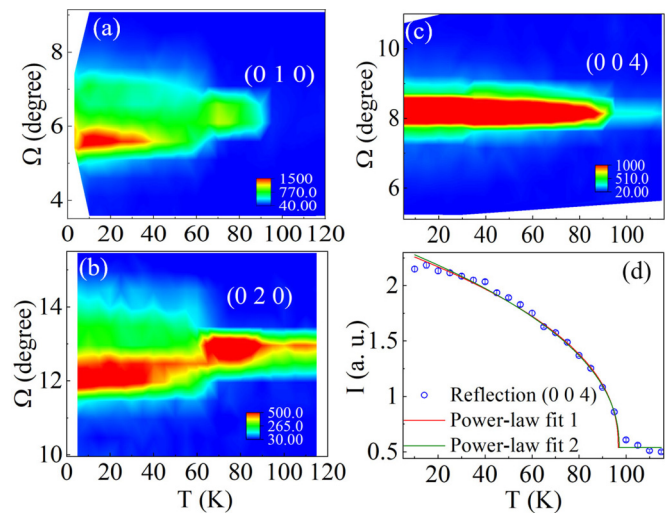


FIG. 7. (a)–(c) Contour plots of the neutron diffraction reflections (0 1 0), (0 2 0), and (0 0 4) as a function of temperature. (d) Temperature dependence of the (0 0 4) peak intensity. The solid lines stand for the power-law fits in different temperature regimes.

by considering the two space groups using AMPLIMODES [33]. The decomposition of the low temperature structure in respect of the symmetrized displacive modes of the parent  $P\bar{3}c1$  structure yields a set of symmetry-adapted distorted modes that are associated with two irreducible representation (irreps) GM1+ (order parameter direction:  $a$ , amplitude: 0.0649 Å) and GM3+ (order parameter direction:  $(-0.5a, 0.866a)$ , amplitude: 0.1124 Å). Through the analysis, we found that GM3+ transforms all the primary modes. We drew the displacements corresponding to each symmetry mode of all O atoms (which form the distorted octahedra  $\text{FeO}_6$ ) in Fig. 6(d) which shows that the largest distortions/displacements occur mainly in the  $ab$  plane.

Although the magnetic structure of  $\text{Fe}_4\text{Nb}_2\text{O}_9$  was previously reported by studying a powder sample using neutron diffraction, the exact magnetic symmetry is still unclear as powder neutron diffraction can not distinguish the magnetic space groups  $C2'/c$  and  $C2/c'$  [26]. We carried out single crystal neutron diffraction on  $\text{Fe}_4\text{Nb}_2\text{O}_9$  to clearly sort out this problem. Even though  $\text{Fe}_4\text{Nb}_2\text{O}_9$  undergoes a crystal structure phase transition at 70 K with splittings of some specific Bragg peaks, no anomaly was observed in the magnetic reflections, indicating that the magnetic symmetry is preserved upon cooling. Therefore, hereafter, we will describe the magnetic structure in the parent structure. As shown in Figs. 7(a) and 7(c), below 97 K, the peak intensities of (0 1 0) and (0 0 4) increase with decreasing temperature, signaling the onset of the magnetic transition. Since reflection (0 0 4) is not contaminated by the crystal structural transition, it was chosen to track the order parameter of the magnetic transition. The reflection (0 0 4) can be fitted by an empirical power-law equation  $I = A \left( \frac{T_N - T}{T_N} \right)^{2\beta} + B$  [34,35] where  $T_N$  is the Néel temperature,  $A$  is a proportionality constant,  $\beta$  is the order parameter critical exponent, and  $B$  is the background. We fitted the intensity in two temperature regimes. In the temperature range of 10–115 K, the fit yields  $T_N = 96.7(5)$  K and a critical exponent 0.216(9), as shown in Fig. 7(d) (power-law fit 1). Fitting the data in the temperature range of 65–115 K [power-law fit 2 in Fig. 7(d)] gives a similar critical exponent 0.23(3). This value is close to the characteristic critical exponent  $\beta = 0.231$  for a two-dimensional XY model [34–36], reflecting that the anisotropy is planar, in good agreement with the spin configuration from the neutron diffraction analysis in the following paragraph. At 5 K, all observed magnetic reflections were well indexed by a vector  $\mathbf{k} = \mathbf{0}$ , consistent with that found in the powder sample [26].

A set of magnetic subgroups that are compatible with the given space group and the propagation vector was obtained through the symmetry analysis using BILBAO CRYSTALLOGRAPHIC SERVER (MAGNETIC SYMMETRY AND APPLICATIONS [33]) software. The magnetic structures containing trigonal symmetry imply a magnetic configuration with the moments along the  $c$ -axis, inconsistent with our experimentally measured magnetic reflections such as (0 0 4) and thermodynamic measurements. Thus, we have to lower the symmetry in the magnetic subgroup hierarchy. This gives four monoclinic magnetic subgroups  $C2'/c'$ ,  $C2/c'$ ,  $C2'/c$ , and  $C2/c$ . Without refining our neutron data, one can rule out the subgroups

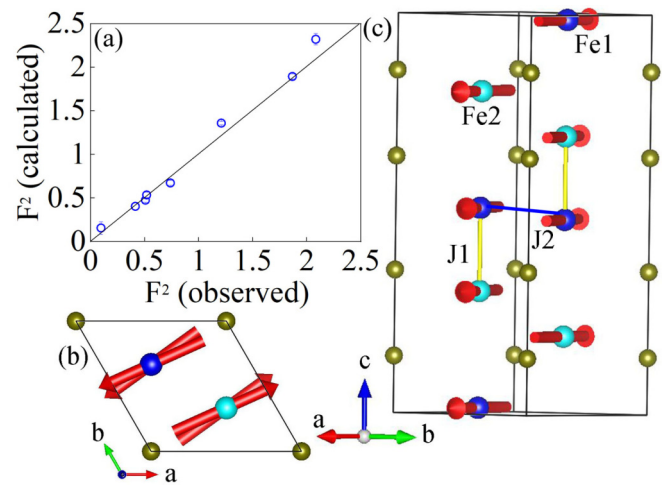


FIG. 8. (a) Observed intensity of all magnetic peaks at 5 K compared to those calculated by fitting the magnetic structural model. (b,c) The ground-state magnetic structure of  $\text{Fe}_4\text{Nb}_2\text{O}_9$  in the hexagonal lattice setting. The solid yellow line marks the nearest-neighbor exchange interaction while the solid blue line represents the next-nearest-neighbor exchange interaction  $J_2$ .

$C2'/c'$  and  $C2/c$  by applying Neumann's principle to the magnetoelectric effect. Basically, both of them do not allow the linear magnetoelectric effect. We tested the remaining magnetic models using the single crystal neutron diffraction data. The model corresponding to the subgroup  $C2'/c'$  yields a satisfactory fit to our data ( $R_F = 4.43\%$  and  $\chi^2 = 5.13$ ), as shown in Fig. 8(a). In fact, another reason of precluding the other candidate  $C2'/c$  is based on the magnetoelectric coupling experimentally observed in  $\text{Fe}_4\text{Nb}_2\text{O}_9$  since the  $C2'/c$  subgroup allows only four off-diagonal terms. Therefore, we can conclude that the magnetic structure of  $\text{Fe}_4\text{Nb}_2\text{O}_9$  is described by the magnetic space group  $C2'/c'$ . Figures 8(b) and 8(c) show the magnetic structure of  $\text{Fe}_4\text{Nb}_2\text{O}_9$ , which is manifested as antiferromagnetically coupled ferromagnetic chains along the  $c$  axis with all spins confined into the  $ab$  plane. In particular, the nearest-neighbor Fe atoms, i.e., Fe1 and Fe2 order ferromagnetically. This pair forms a small canting angle  $5.81^\circ$  with its adjacent Fe1-Fe2 pair in the chain. This canting angle is roughly two times smaller than that in  $\text{Co}_4\text{Nb}_2\text{O}_9$  [23]. The refined magnetic moment at 5 K is  $3.52(4) \mu_B$  for both the Fe1 and Fe2 sites. This value is slightly smaller than the theoretical ordered spin-only value  $4 \mu_B$  for  $\text{Fe}^{2+}$  with a high spin state. Due to the existence of the trigonal lattice symmetry, three magnetic domains were considered and their populations were set to be equal during the refinement.

#### IV. DISCUSSION

We established that  $\text{Fe}_4\text{Nb}_2\text{O}_9$  undergoes an antiferromagnetic phase transition around 97 K, followed by a structural transition at 70 K. By combining x-ray and neutron diffraction, we solved the crystal structure and magnetic symmetry at low temperatures. The magnetic structure is featured by the ferromagnetic chain with a small canting between each adjacent Fe1-Fe2 pair. This indicates that the dominant

exchange interaction  $J_1$  is ferromagnetic. Owing to the presence of the antiferromagnetic exchange interactions ( $J_2$ ) between Fe1 atoms in the slightly buckled honeycomb, the ferromagnetic chains are coupled antiferromagnetically. The strong competition between the two sorts of exchange interactions is likely responsible for the small canting angle between each ferromagnetic Fe1-Fe2 pair. The magnetoelectric coupling of  $\text{Fe}_4\text{Nb}_2\text{O}_9$  can be appreciated by symmetry analysis in light of the determined magnetic structure. Imposed by the magnetic symmetry  $C2/c'$ , the magnetoelectric coupling tensor has in principle five nonzero terms:  $\alpha_{xx}$ ,  $\alpha_{xz}$ ,  $\alpha_{yy}$ ,  $\alpha_{zx}$ ,  $\alpha_{zz}$ . Our magnetodielectric and electric polarization measurements along the different directions of the crystal have shown that the strongest term is  $\alpha_{zx}$  and the term  $\alpha_{xx}$  is small while the term  $\alpha_{zz}$  is null. The off-diagonal component  $\alpha_{zx}$  with a large value in principle allows the occurrence of the ferrotoroidal order in  $\text{Fe}_4\text{Nb}_2\text{O}_9$ . The experimental observation of the relevant ferrotoroidal domains through an essential magnetoelectric annealing process is greatly desired.

Let us discuss the dielectric anomalies in  $\varepsilon'(T)$  curves without the magnetic field. In the vicinity of the magnetic phase transition, the dielectric anomaly was observed in  $\varepsilon'_a(T)$ , indicating a strong correlation between the spin ordering and the dielectric properties in  $\text{Fe}_4\text{Nb}_2\text{O}_9$ . Its absence in  $\varepsilon'_c(T)$  further reflects that it is governed by exchange interactions in the  $ab$  plane. This is associated with the fact that all magnetic moments are confined in the  $ab$  plane. A dielectric anomaly near the magnetic phase transition has also been previously found in the isostructural  $\text{Co}_4\text{Nb}_2\text{O}_9$  [37] in which the dielectric constant monotonically increases from the magnetic ordering temperature to 10 K (the lowest measured temperature) with about 0.2% increment. Different from  $\text{Fe}_4\text{Nb}_2\text{O}_9$ , this small dielectric response is field-dependent, suggesting different origins. Similar dielectric anomalies to  $\text{Fe}_4\text{Nb}_2\text{O}_9$  were found in a diversity of antiferromagnets including classical antiferromagnetic MnO [38] and  $\text{MnF}_2$  [39], linear magnetoelectric  $\text{BaMnF}_4$  [40] and  $\text{NdCrTiO}_5$  [41], multiferroic  $\text{TbFe}_3(\text{BO}_3)_4$  [42],  $\text{YMnO}_3$  and  $\text{LuMnO}_3$  [43,44], magnetoelectric  $\text{Pb}_2\text{MnO}_4$  [45], and quantum paraelectric  $\text{EuTiO}_3$  [46]. As shown in Fig. 9, ferroelectric  $\text{TbFe}_3(\text{BO}_3)_4$  [42],  $\text{YMnO}_3$  and  $\text{LuMnO}_3$  [43,44] show a dielectric drop in the range of 3–5% near their spin ordering temperatures. This was believed to arise from the coupling between the polar modes and the magnetic ordering. A comparable dielectric drop  $\sim 3.75\%$  near the magnetic ordering temperature has been reported in the incipient ferroelectric  $\text{EuTiO}_3$  [46]. The low-temperature dielectric constant of  $\text{EuTiO}_3$  significantly increases with the decrease of temperature and saturates with a large dielectric constant  $> 400$  below approximately 30 K due to a soft mode type incipient ferroelectric behavior [46]. Its dielectric drop below 5.5 K was attributed to the coupling between the soft polar phonon mode and the localized Eu spins which allows a third-order magnetoelectric effect as confirmed experimentally [47]. In contrast to these ferroelectric materials, the dielectric constant  $\varepsilon'_a$  and  $\varepsilon'_c$  of  $\text{Fe}_4\text{Nb}_2\text{O}_9$  monotonically decrease with decreasing temperature and show a rather smaller dielectric constant ( $\varepsilon'_a \sim 40$ ) around  $T_N$ .  $\text{Fe}_4\text{Nb}_2\text{O}_9$  has a significantly larger dielectric response ( $\sim 40\%$  drop) and stands out as a unique case. This makes  $\text{Fe}_4\text{Nb}_2\text{O}_9$  evidently different from the incipient

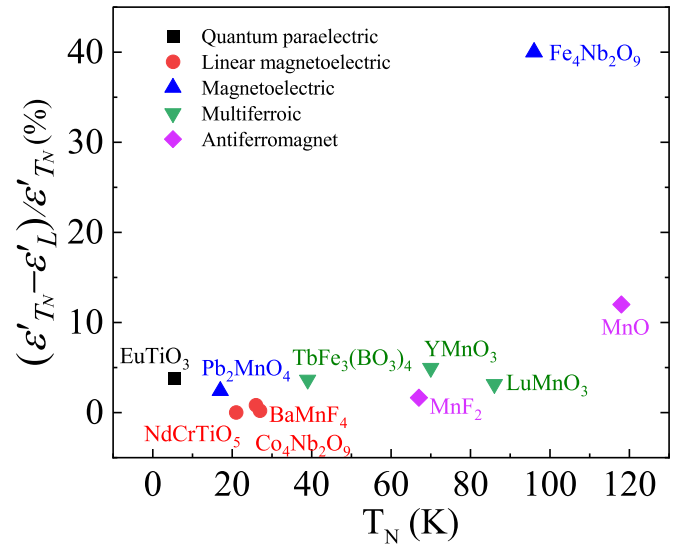


FIG. 9. The dielectric change below  $T_N$  due to spin ordering in representative antiferromagnetic materials. Note that the dielectric change was evaluated using  $(\varepsilon'_{T_N} - \varepsilon'_L) / \varepsilon'_{T_N}$  where  $\varepsilon'_L$  is the static dielectric constant at the lowest measured temperature for each case.

ferroelectric  $\text{EuTiO}_3$ . Note that due to the lack of a coupled soft phonon mode, the third-order ME effect is unlikely to occur in  $\text{Fe}_4\text{Nb}_2\text{O}_9$ . However,  $\text{Fe}_4\text{Nb}_2\text{O}_9$  shares considerable similarities in dielectric properties with MnO which shows a decrease of the dielectric permittivity with  $\sim 12\%$  below  $T_N$  and was explained by the presence of exchange striction due to the structural distortions driven by nearest-neighbor and next-nearest-neighbor antiferromagnetic interactions [38]. We found that the slope change in the dielectric constant curve in  $\text{Fe}_4\text{Nb}_2\text{O}_9$  is analogous to that observed in MnO where the anomalous dielectric contribution below the Néel temperature is proportional to  $M^2$  ( $M$  is the sublattice magnetization) [38]. We evaluated this proportionality. In  $\text{Fe}_4\text{Nb}_2\text{O}_9$ , the anomalous dielectric contribution can not be quantitatively evaluated since modeling the high temperature dielectric constant needs a comprehensive knowledge of the lattice polarizability [38]. However, because the lattice contribution at low temperatures is practically temperature-independent, it is not unreasonable to directly compare the dielectric constant and the magnetization below  $T_N$ . Figure 10 shows the comparison between the dielectric constant and the intensity of the magnetic reflection (0 0 4). It is obvious that both curves are approximately proportional. This reflects that the occurrence of the dielectric anomaly exclusively in the  $\varepsilon'_a$  below  $T_N$  is likely due to the exchange striction. Another anomaly in the dielectric constant curve around  $T_S = 70$  K featured by the thermal hysteresis is associated with the first-order crystal structure transition. As shown in Fig. 6(d), the symmetry mode analysis of the lower temperature phase with respect to the high-temperature phase gives significant O atomic displacements in the  $ab$  plane. Such a structural distortion unsurprisingly varies the dielectric constants. However, as we shown in Fig. 10, it is the magnetic ordering that dominates the formation of the giant dielectric response.

The nature of the exchange striction in  $\text{Fe}_4\text{Nb}_2\text{O}_9$  is unclear. Usually, it is accompanied by structural distortions

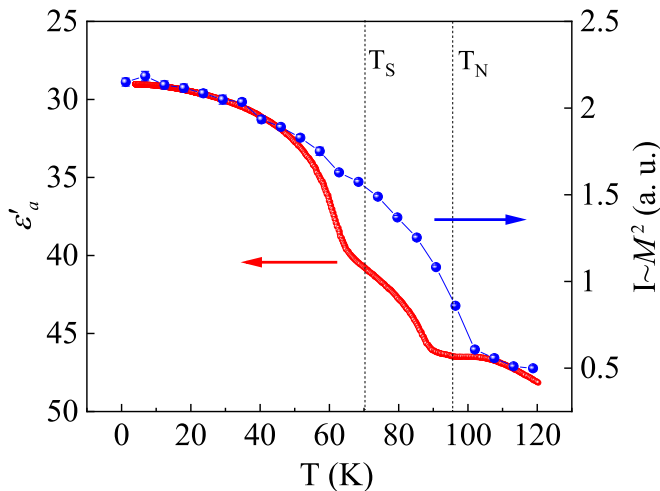


FIG. 10. Comparison between the dielectric constant  $\epsilon'_a(T)$  and the magnetic reflection (0 0 4) as a function of temperature. Note the peak intensity is proportional to the square of the magnetic moment in  $\text{Fe}_4\text{Nb}_2\text{O}_9$ .

or changes of the lattice dimension. However, such distortions may be small and local and cannot be observed by conventional diffraction methods. The total neutron scattering technique as a complementary tool has been used to successfully resolve the distorted crystal structure associated with the magnetic ordering in MnO using the reverse Monte Carlo method [48]. In this sense, high-resolution total neutron scattering experiments are needed to understand the dielectric anomaly in  $\text{Fe}_4\text{Nb}_2\text{O}_9$ . In addition, the origin of the structural phase transition appears to be associated with the magnetic ordering. The magnetic space group of  $\text{Fe}_4\text{Nb}_2\text{O}_9$  is  $C2/c'$  which is identical, irrespective of the time reversal operator, to the lower temperature crystal structure  $C2/c$ . This poses a speculation that an “incipient” structural phase transition occurs at  $T_N$ , that may be related to the change of the frequency of some specific modes or phonon splittings due to the magnetic ordering [49]. Further inelastic neutron scattering by mapping out the phonon dispersion across the magnetic and structural phase transitions will be helpful to address this point.

## V. CONCLUSION

In summary, we studied the dielectric properties, the magnetoelectric coupling, and the magnetic structure of  $\text{Fe}_4\text{Nb}_2\text{O}_9$ . The magnetic susceptibility and single crystal neutron diffraction showed an antiferromagnetic transition around 97 K described by the  $C2/c'$  magnetic space group with two antiparallel ferromagnetic chains totally confined in the  $ab$  plane. Along the  $c$  axis, a small but pivotal canting angle between each adjoining Fe1-Fe2 atoms was found. This magnetic symmetry probably triggers the occurrence of exchange striction that explains the large anomaly ( $\sim 40\%$  drop) in the dielectric constant curve in the  $a$  direction, and allows the linear ME effect as observed experimentally by the magnetodielectric response and electric polarization measurements. A hexagonal to monoclinic structural transition at  $T_S = 70$  K has been revealed by combining neutron and x-ray single crystal diffraction and symmetry-adapted mode analysis. Our work suggests that manipulation of the magnetoelectric coupling through an external magnetic field is practicable since the magnetic configuration in honeycomb  $\text{Fe}_4\text{Nb}_2\text{O}_9$  makes the continuous rotation of the moments via a magnetic field robust.

## ACKNOWLEDGMENTS

The research at Oak Ridge National Laboratory (ORNL) was supported by the U.S. Department of Energy (DOE), Office of Science, Office of Basic Energy Sciences, Early Career Research Program Award KC0402010, under Contract DE-AC05-00OR22725. This research used resources at the High Flux Isotope Reactor, a DOE Office of Science User Facility operated by ORNL. The work at the University of Tennessee was supported by DOE under award DE-SC-0020254. A portion of this work was performed at the National High Magnetic Field Laboratory, supported by the National Science Foundation Cooperative Agreement No. DMR-1644779 and the State of Florida. The work at Chongqing University was supported by the Fundamental Research Funds for the Central Universities (2020CDJQY-A056, 2018CDJDWL0011) and Projects of President Foundation of Chongqing University (2019CDXZWL002).

- [1] H. Schmid, *Ferroelectrics* **162**, 317 (1994).
- [2] J.-P. Rivera, *Eur. Phys. J. B* **71**, 299 (2009).
- [3] M. Fiebig, *J. Phys. D* **38**, R123 (2005).
- [4] Y. Tokura, S. Seki, and N. Nagaosa, *Rep. Prog. Phys.* **77**, 076501 (2014).
- [5] N. A. Spaldin, M. Fiebig, and M. Mostovoy, *J. Phys.: Condens. Matter* **20**, 434203 (2008).
- [6] H. Schmid, *J. Phys.: Condens. Matter* **20**, 434201 (2008).
- [7] J. Wang, J. B. Neaton, H. Zheng, V. Nagarajan, S. B. Ogale, B. Liu, D. Viehland, V. Vaithyanathan, D. G. Schlom, U. V. Waghmare, N. A. Spaldin, K. M. Rabe, M. Wuttig, and R. Ramesh, *Science* **299**, 1719 (2003).
- [8] N. A. Spaldin, M. Fiebig, *Science* **309**, 391 (2005).
- [9] W. Eerenstein, N. D. Mathur, and J. F. Scott, *Nature (London)* **442**, 759 (2006).
- [10] S.-W. Cheong and M. Mostovoy, *Nat. Mater.* **6**, 13 (2007).
- [11] L. Ding, C. V. Colin, C. Darie, J. Robert, F. Gay, and P. Bordet, *Phys. Rev. B* **93**, 064423 (2016).
- [12] E. Fischer, G. Gorodetsky, and R. M. Hornreich, *Solid State Commu.* **10**, 1127 (1972).
- [13] N. D. Khanh, N. Abe, H. Sagayama, A. Nakao, T. Hanashima, R. Kiyonagi, Y. Tokunaga, and T. Arima, *Phys. Rev. B* **93**, 075117 (2016).
- [14] E. F. Bertaut, L. Corliss, F. Forrat, R. Aleonard, and R. Pauthenet, *J. Phys. Chem. Solids* **21**, 234 (1961).
- [15] I. E. Dzyaloshinskii, *Zh. Exp. Teor. Fiz.* **37**, 881 (1959) [*Sov. Phys. JETP* **10**, 628 (1960)].

- [16] D. N. Astrov, *Zh. Exp. Teor. Fiz.* **38**, 984 (1960) [Sov. Phys. JETP **11**, 708 (1960)].
- [17] A. Iyama and T. Kimura, *Phys. Rev. B* **87**, 180408(R) (2013).
- [18] M. Fiebig, D. Frohlich, B. B. Krichevtsov, and R. V. Pisarev, *Phys. Rev. Lett.* **73**, 2127 (1994).
- [19] T. R. McGuire, E. J. Scott, and F. H. Grannis, *Phys. Rev.* **102**, 1000 (1956).
- [20] Y. Fang, W. P. Zhou, S. M. Yan, R. Bai, Z. H. Qian, Q. Y. Xu, D. H. Wang, and Y. W. Du, *J. Appl. Phys.* **117**, 17B712 (2015).
- [21] Y. Fang *et al.*, *Sci. Rep.* **4**, 3860 (2014).
- [22] N. D. Khanh, N. Abe, S. Kimura, Y. Tokunaga, and T. Arima, *Phys. Rev. B* **96**, 094434 (2017).
- [23] L. Ding *et al.*, [arXiv:2002.10599](https://arxiv.org/abs/2002.10599).
- [24] G. Deng, Y. Cao, W. Ren, S. Cao, A. J. Studer, N. Gauthier, M. Kenzelmann, G. Davidson, K. C. Rule, J. S. Gardner, P. Imperia, C. Ulrich, and G. J. McIntyre, *Phys. Rev. B* **97**, 085154 (2018).
- [25] A. Maignan and C. Martin, *Phys. Rev. B* **97**, 161106(R) (2018).
- [26] R. Jana, D. Sheptyakov, X. Ma, J. A. Alonso, M. Pi, A. Muñoz, Z. Liu, L. Zhao, N. Su, S. Jin, X. Ma, K. Sun, D. Chen, S. Dong, Y. Chai, S. Li, and J. Cheng, *Phys. Rev. B* **100**, 094109 (2019).
- [27] Rigaku (2005). CrystalClear. Rigaku Corporation, Tokyo, Japan.
- [28] T. Higashi, ABSCOR (2000). Rigaku Corporation, Tokyo, Japan.
- [29] J. Rodriguez-Carvajal, *Physica B* **192**, 55 (1993).
- [30] B. C. Chakoumakos, H. Cao, F. Ye, A. D. Stoica, M. Popovici, M. Sundaram, W. Zhou, J. S. Hicks, G. W. Lynn, and R. A. Riedel, *J. Appl. Cryst.* **44**, 655 (2011).
- [31] C. Heid, H. Weitzel, F. Bourdarot, R. Calemczuk, T. Vogt, and H. Fuess, *J. Phys.: Condens. Matter* **8**, 10609 (1996).
- [32] N. Mufti, G. R. Blake, M. Mostovoy, S. Riyadi, A. A. Nugroho, and T. T. M. Palstra, *Phys. Rev. B* **83**, 104416 (2011).
- [33] J. M. Perez-Mato, S. V. Gallego, E. S. Tasci, L. Elcoro, G. de la Flor, and M. I. Aroyo, *Annu. Rev. Mater. Res.* **45**, 217 (2015).
- [34] L. J. de Jongh and A. R. Miedema, *Adv. Phys.* **23**, 1 (1974).
- [35] S. T. Bramwell and P. C. W. Holdsworth, *J. Phys.: Condens. Matter* **5**, L53 (1993).
- [36] A. Taroni, S. T. Bramwell, and P. C. W. Holdsworth, *J. Phys.: Condens. Matter* **20**, 275233 (2008).
- [37] Y. M. Xie, C. S. Lin, H. Zhang, and W. D. Cheng, *AIP Adv.* **6**, 045006 (2016).
- [38] M. S. Seehra and R. E. Helmick, *Phys. Rev. B* **24**, 5098 (1981).
- [39] M. S. Seehra and R. E. Helmick, *J. Appl. Phys.* **55**, 2330 (1984).
- [40] J. F. Scott, *Phys. Rev. B* **16**, 2329 (1977).
- [41] J. Hwang, E. S. Choi, H. D. Zhou, J. Lu, and P. Schlottmann, *Phys. Rev. B* **85**, 024415 (2012).
- [42] U. Adem, L. Wang, D. Fausti, W. Schottenhamel, P. H. M. van Loosdrecht, A. Vasiliev, L. N. Bezmaternykh, B. Buchner, C. Hess, and R. Klingeler, *Phys. Rev. B* **82**, 064406 (2010).
- [43] Z. J. Huang, Y. Cao, Y. Y. Sun, Y. Y. Xue, and C. W. Chu, *Phys. Rev. B* **56**, 2623 (1997).
- [44] T. Katsufuji, S. Mori, M. Masaki, Y. Moritomo, N. Yamamoto, and H. Takagi, *Phys. Rev. B* **64**, 104419 (2001).
- [45] D. C. Kakarla, H. C. Wu, D. J. Hsieh, P. J. Sun, G. J. Dai, J. -Y. Lin, J. L. Her, Y. H. Matsuda, L. Z. Deng, M. Gooch, C. W. Chu, and H. D. Yang, *Phys. Rev. B* **99**, 195129 (2019).
- [46] T. Katsufuji and H. Takagi, *Phys. Rev. B* **64**, 054415 (2001).
- [47] V. V. Shvartsman, P. Borisov, W. Kleemann, S. Kamba, and T. Katsufuji, *Phys. Rev. B* **81**, 064426 (2010).
- [48] A. L. Goodwin, M. G. Tucker, M. T. Dove, and D. A. Keen, *Phys. Rev. Lett.* **96**, 047209 (2006).
- [49] Ch. Kant, M. Schmidt, Z. Wang, F. Mayr, V. Tsurkan, J. Deisenhofer, and A. Loidl, *Phys. Rev. Lett.* **108**, 177203 (2012).